Research Article

The Complex Story Behind a Deep Eutectic Solvent Formation as Revealed by L-Menthol Mixtures with Butylated Hydroxytoluene Derivatives

Matteo Busato,* Giorgia Mannucci, Lorenzo Augusto Rocchi, Maria Enrica Di Pietro,
Angela Capocefalo, Elisa Zorzi, Paolo Casu, Daniele Veclani, Franca Castiglione, Andrea Mele,
Andrea Martinelli, Paolo Postorino, and Paola D'Angelo*

Cite This: ACS Sustainable Chem. Eng. 2023, 11, 8988−8999

Read Online

ACCESS | Metrics & More | Article Recommendations | Supporting Information

ABSTRACT: An in-depth study of the hydrophobic eutectic mixtures formed by L-menthol (MEN) with the butylated hydroxytoluene (BHT), 2-*tert*-butyl-*p*-cresol (TBC), and *p*-cresol (PC) compounds has been carried out, where TBC and PC are analogous to the BHT species but with a different degree of steric hindrance around the hydroxyl group. Thermal characterization evidenced that the BHT/MEN system can be classified as an ideal eutectic, while the TBC/MEN and PC/MEN mixtures behave as type V deep eutectic solvents (DESs) for a wide range of compositions around the eutectic point. As shown by an array of experimental and theoretical methods, in the BHT/MEN mixtures the establishment of hydrogen-bond (H-bond) interactions between the components is dramatically hampered because of the steric hindrance in the BHT molecule, so that the achievement of a liquid phase at room temperature for the eutectic composition is driven by apolar−apolar attractions among the alkyl functional groups of the constituents. Differently, the TBC-MEN donor−receptor H-bond is the main driving force for the formation of a type V DES and derives from a concurrence of electronic and steric factors characterizing the TBC molecule. Finally, the absence of steric hindrance around the hydroxyl group allows the self-association among PC molecules through H-bonded networks already in the pristine compound, but the replacement with the more favorable PC-MEN H-bond provides a type V DES upon mixing of these components. Our combined approach, together with the peculiarity of the inspected systems, delivered an archetypal study able to shed light onto the various contributions ruling the structure−properties relationship in DESs and possibly deepening the currently accepted view of these inherently complex media.

KEYWORDS: Hydrophobic deep eutectic solvents, menthol, butylated hydroxytoluene, differential scanning calorimetry, Raman spectroscopy, NMR, molecular dynamics
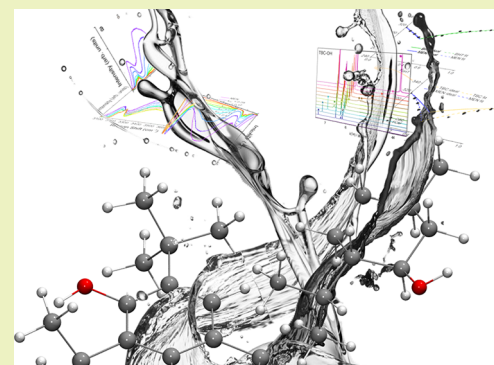
INTRODUCTION

Deep eutectic solvents (DESs) are currently the ruling research topic about alternative media to traditional solvents owing to key properties like simple preparation, no need for purification, versatility, and an environmentally benign pedigree.[1−3] DESs also belong to the "designer" solvents category, meaning that their chemico-physical properties can be tuned to meet specific requirements through a judicious choice of the precursors and of their relative composition.[1] These qualities can potentially provide materials ideally suited for application fields among which the energy production and storage,[4,5] electroplating,[6,7] separation procedures,[8,9] CO_2 sequestration,[10] catalytic processes,[11,12] and drug delivery[13,14] represent a long but inevitably spurious list. The definition of these systems has been for a long time a source of debate in the scientific community, but at present an agreement seems to have been found in defining DESs as mixtures of two or more compounds showing a melting point (MP) depression that is significantly deeper than the ideally predicted one for at least one composition.[15,16] Moreover, the MP of the eutectic is lower than those of the individual parent compounds, thus allowing the achievement of a liquid phase even from solid starting materials. This behavior was described for the first time by Abbott and co-workers, who reported that by mixing choline chloride and urea, both solids at room temperature, a liquid phase with an MP of 12 °C was obtained for the 1:2 molar ratio, which was called "reline".[17] Nevertheless, the extent of
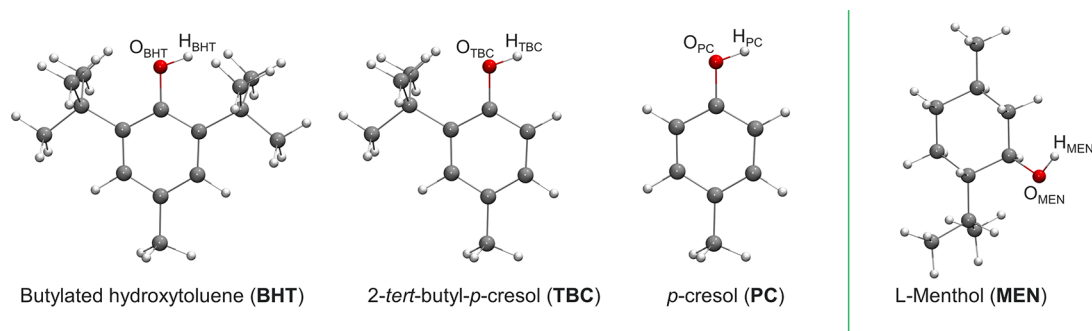
Figure 1. Molecular structures of the butylated hydroxytoluene (BHT), 2-*tert*-butyl-*p*-cresol (TBC), *p*-cresol (PC), and ʟ-menthol (MEN) components within the employed atom nomenclature (white, hydrogen; gray, carbon; red, oxygen).

deviation from thermal ideality required to provide a "true" DES remains an ambiguous task.

The majority of the currently available DESs, classified in the type I−IV categories, is formed by at least one ionic component, so that the origin of the MP depression is typically attributed to complexation of a hydrogen-bond (H-bond) acceptor from a H-bond donor.[2,3,18−24] More recently, type V DESs have been presented and are formed by neutral molecular components only, very often based on terpenoid compounds like menthol and thymol.[25,26] Being nonionic, they typically display lower viscosities, are chloride-free, and often hydrophobic, so that they are suited for the removal of target analytes from aqueous solutions through liquid−liquid biphasic extractions.[27−29] However, also, this category deals with species possessing H-bonding capabilities. For these reasons, DESs are often indicated as extensively H-bonded media, which, although not being a strict definition for these systems, has become a common way to identify them. Examples of alternative interactions concurring as a driving force for the MP depression are scarce in the literature and only consist of a few cases pointing out the establishment of halogen or chalcogen bonding between the components,[30−32] while apolar−apolar attractions led by dispersion interactions have also been invoked[1−3,33] but never clearly demonstrated.

In this way, many key scientific questions remain unanswered. On the one hand, the individuation of H-bonding as the only parameter to take into account in DESs' designing seems to start crackling, even if the overwhelming literature about salt-based DESs condemns this argument as still being in its infancy. On the other hand, the achievement of a clearer predictive understanding of the structure−property relationship necessary to design new task-specific DESs is a legitimate goal. Here, we start answering these questions by proposing an extensive study about the mixtures formed by ʟ-menthol (MEN) with the butylated hydroxytoluene (BHT), 2-*tert*-butyl-*p*-cresol (TBC), and *p*-cresol (PC) compounds (Figure 1). It was recently demonstrated that mixing of BHT and MEN at a 1:3 molar ratio (or, equivalently, at BHT molar fraction x_{BHT} = 0.25) provides a liquid phase at room temperature suitable for liquid−liquid microextractions of pesticides and fat-soluble micronutrients from food matrices.[34,35] This system is very intriguing as the molecular structure of BHT shows an evidently encumbered hydroxyl group because of two adjacent *tert*-butyl substituents (Figure 1).[36−39] Given that the hydroxyl group should be the main thing responsible for the H-bond interaction, we decided to study also MEN mixtures with TBC and PC counterparts, which are analogues of BHT but with respectively one and no

tert-butyl groups in *ortho*-position to the hydroxyl. Note that the PC compound possesses acute toxicity, so that the PC/MEN mixtures are far from meeting the requirements of sustainable solvents, but it was selected to solve the scientific case as it is the structural analogue species to the BHT and TBC ones but with no steric hindrance around the hydroxyl group. In this way, BHT/MEN, TBC/MEN, and PC/MEN mixtures covering the full composition range of the components have been studied with an array of complementary experimental and theoretical methods able to deliver information from the molecular length-scale aggregation to the macroscopic behavior. The employed techniques include thermal analysis aimed at building solid−liquid equilibrium (SLE) diagrams by means of differential scanning calorimetry (DSC) and polarized optical microscopy (POM), proton (^{1}H) nuclear magnetic resonance (NMR) and Raman spectroscopy, and molecular dynamics (MD) simulations at both the classical and density functional tight-binding (DFTB-MD) levels of theory. Altogether, our combined methods and the peculiarity of the chosen systems provided an archetypal study able to shed light onto various steric and electronic contributions influencing the structure−property correlation in DESs. The impact of this work is that of providing new tools for a more conscious DES design and to possibly expand the currently accepted view of these systems.

■ METHODS

Chemicals and Sample Preparation. MEN (natural source, food grade, ≥99%) and BHT (food grade, ≥99%) were purchased from Merck Life Science S.r.l. (Milan, Italy), while TBC (≥98%) and PC (≥99%) came from TCI EUROPE N.V. (Zwijndrecht, Belgium) and were used as received. BHT/MEN, TBC/MEN, and PC/MEN mixtures at different molar fractions x_{BHT}, x_{TBC}, and x_{PC} of the components covering the full composition range at ∼0.1 intervals were prepared by mixing the desired amount of the pristine compounds in glass test tubes and heating at 343 K until homogeneous liquids were obtained. The samples were then stored in glass sealed vials at room temperature before the measurements. Under these conditions, crystallization was observed for the systems whose MP was above room temperature, which were melted again before the withdrawal for the instrumental measurements. The full list of the prepared samples is reported in Table S1 of the Supporting Information (SI).

DSC and POM Experiments. The MPs of the various BHT/MEN, TBC/MEN, and PC/MEN mixtures were determined by means of DSC and POM measurements to build the SLE diagrams for these systems. DSC thermograms were acquired with a Mettler Toledo DSC 822e differential calorimeter (Mettler Toledo, Greifensee, Switzerland), equipped with a ceramic FRS5 sensor and a liquid nitrogen cooler. A sample quantity of 5−10 mg was sealed in

a 40 μL aluminum pan and subjected to a temperature program consisting of a first cooling ramp at -2 K min^{-1} from 353 to 193 K, followed by a heating ramp from 193 to 353 at 1 K min^{-1}. During the measurements, the furnace was purged with dry nitrogen with a flow rate of 30 mL min^{-1}. The MP of each mixture was taken as the maximum value of the melting peak occurring at the highest temperature in the heating ramp.

POM analysis was performed on the samples showing no melt or cold crystallization during the cooling or heating scans in the DSC experiments (*vide infra*). An Optiphot2-Pol light microscope (Nikon) equipped with a Linkam HFS 91 hot stage was employed, driven by a Linkam TP 92 temperature controller and connected to a digital camera (Nikon D5000). All of the experiments were carried out under a N$_2$ flow. A sample quantity of about 10 mg was positioned on a glass slide, and the temperature program consisted of a first cooling ramp from 353 to 173 K at -90 K min^{-1}, followed by a heating ramp from 193 to 353 K at 5 K min^{-1}. The MP of each mixture was taken as the average temperature between the start and the end point of the crystal melting process. For the sake of comparison with the DSC results, POM measurements were carried out in the whole composition range.

Details about the building of the SLE phase diagrams are given in the SI.

Raman Spectroscopy Measurements. Raman spectra were collected at the HPS laboratory of Sapienza University of Rome using a Horiba HR-Evolution microspectrometer in backscattering geometry equipped with a solid state laser (λ = 532 nm, 90 mW power at the sample surface) and a set of neutral attenuating optical filters to avoid laser heating and sample degradation. The elastically scattered light was removed by a state-of-the-art optical filtering device based on three BragGrate notch filters,[40] which also allowed us to reach very low frequencies (down to $\sim$50 cm^{-1} from the laser line). The detector was a Peltier-cooled charge-coupled device (CCD), and the spectral resolution was better than 3 cm^{-1} thanks to a 600 groove/mm grating with an 800 mm focal length. The spectrometer was coupled with a confocal microscope supplied with a set of interchangeable objectives. To obtain the best signal-to-noise ratio, an objective with 20$\times$ magnification and an N.A. of 0.35 was employed to collect the full spectra in the 50$-$4500 cm^{-1} range. Raman spectra in the O$-$H stretching (ν_{OH}) region (3100$-$3800 cm^{-1}) were collected with an acquisition time of 50 s. The measurements were carried out by including the liquid samples in a 1 mm quartz cuvette at 323 K thanks to a Peltier thermostated cell to ensure that the samples remained at the liquid state. The data on BHT were collected on a supersaturated solution in *n*-heptane, since the MP of the compound was above the temperature allowed by the instrumental setup. This solvent was chosen as it is expected to give no interference in the ν_{OH} spectral region. For the same reason, data on the BHT/MEN mixtures were acquired only up to the x_{BHT} = 0.70 sample. A polynomial baseline subtraction has been applied to all the spectra.

NMR Spectroscopy. All samples were transferred into 5 mm NMR tubes, equipped with a capillary containing deuterated dimethyl sulfoxide (DMSO-d_6), and then flame-sealed. NMR measurements were performed at 343 K to ensure that all samples were at the liquid state, without sample spinning with a Bruker NEO 500 console (11.74 T) equipped with a direct observe BBFO (broadband including fluorine) iProbe and a variable-temperature unit. The instrument was carefully tuned, shimmed, and the 90° pulses calibrated. For all samples, 1D ^{1}H spectra were recorded with 32 scans using 32 768 points.

Computational Details. Classical MD simulations have been carried out on BHT/MEN, TBC/MEN, and PC/MEN systems covering the full composition range. Cubic boxes were built with $\sim$50 Å side lengths and a number of species chosen to reproduce the simulated density at 343 K. This temperature was chosen to ensure that all samples were in the liquid state. Simulations for density estimation were carried out on systems built starting from the experimental densities at 298 K for the samples with $x_{BHT/TBC/PC}$ = 0.25 and resulting in 0.902, 0.955, and 0.966 g cm^{-3}, respectively. NPT simulations were carried out at 1 atm and 343 K for 10 ns employing the Nosé$-$Hoover thermostat with a relaxation constant of

0.5 ps and the Parrinello$-$Rahman barostat with a coupling constant of 1.0 ps. New simulation boxes were built with random atomic positions with the Packmol program[41] in accordance with the obtained densities, which are listed in Table S3 together with the systems details. After an energy minimization, each box was equilibrated under NVT conditions at 500 K for 20 ns and then simulated for data collection at 343 K for an additional 50 ns. The equations of motion were integrated with a leapfrog algorithm with a 1.0 fs time step, and coordinates were saved every 100 steps. Stretching vibrations involving hydrogen atoms were constrained with the LINCS algorithm.[42] Structures and interactions of the BHT, TBC, and PC molecules were represented with the all-atom optimized potentials for liquid simulations (OPLS-AA) force field,[43] while for the MEN, the OPLS-compatible parameters developed by Jasik et al. were employed.[44] Mixed terms were constructed with the Lorentz$-$Berthelot combining rules, and a cutoff radius of 12 Å was applied for all nonbonded interactions, while long-range electrostatic forces were taken into account with the particle mesh Ewald method.[45,46] Simulations were performed with the Gromacs 2020.2 program,[47] while the VMD 1.9.3 software[48] was used for trajectories visualization and the TRAVIS code for the analysis.[49]

DFTB-MD simulations of the BHT/MEN, TBC/MEN, and PC/MEN systems at the $x_{BHT/TBC/PC}$ = 0.25 composition were carried out using the DFTB+ 21.2 program[50] at the third order variant of the density functional tight-binding (DFTB3) level of theory, which was previously demonstrated to improve the description of H-bond interactions,[51−53] in combination with the third-order-parametrization for organic and biological systems (3OB)[54] Slater$-$Koster files. Cubic boxes were initially built with random positions with the Packmol program,[41] with the size according to the experimental density at 298 K. The systems details are listed in Table S4. For each box, a geometry optimization was carried out and followed by a 2 ps NVE run and 10 ps NVT equilibration at 500 K. 100 ps NVT runs for data collection were carried out at 298 K. Such a relatively long simulation time for an *ab initio* MD simulation was possible thanks to the $\sim$2$-$3 orders of magnitude faster DFTB Hamiltonian than for the full DFT approach.[55] Self-consistent charge (SCC) optimization was carried out with 10^{-5} tolerance, and the *k*-points meshes corresponded to a Γ-point sampling, while periodic boundary conditions were applied in all directions. Thermalization was performed with the Nosé$-$Hoover thermostat with a coupling strength of 3200 cm^{-1}. The equations of motion were integrated with a velocity Verlet algorithm with a 1.0 fs time step and trajectories saved every 10 steps. Grimme's DFT-D4 empirical dispersion corrections were applied to improve the description of van der Waals interactions.[56] The BHT, TBC, PC, and MEN pristine compounds were also simulated with the same level of theory. Production runs for data collection were performed in NVT conditions at 348 K for 50 ps. This temperature was chosen as above the determined MP of BHT (343 K). Details about these systems are listed in Table S5.

RESULTS AND DISCUSSION

Thermal Characterization. Access to the SLE phase diagram between the components is imperative for the thermodynamic characterization of a eutectic mixture, as it allows one to compare the experimental MP depression to the ideally predicted one and classify a system as either a DES or a eutectic solvent. In Figure 2, we report the phase diagrams for the BHT/MEN, TBC/MEN, and PC/MEN mixtures, where the best-fit curves obtained after interpolation of the experimental MP temperatures are compared with the ideal SLE diagrams. Table 1 lists the eutectic point compositions and melting temperatures, together with the effective interaction parameter χ obtained after the interpolation procedure (see the SI for details and meaning of the χ parameter). For the BHT/MEN system (Figure 2a), both the ideal and experimental eutectic points occur at x_{BHT} = 0.29. For this composition, an MP of 295.5 K is predicted, while the
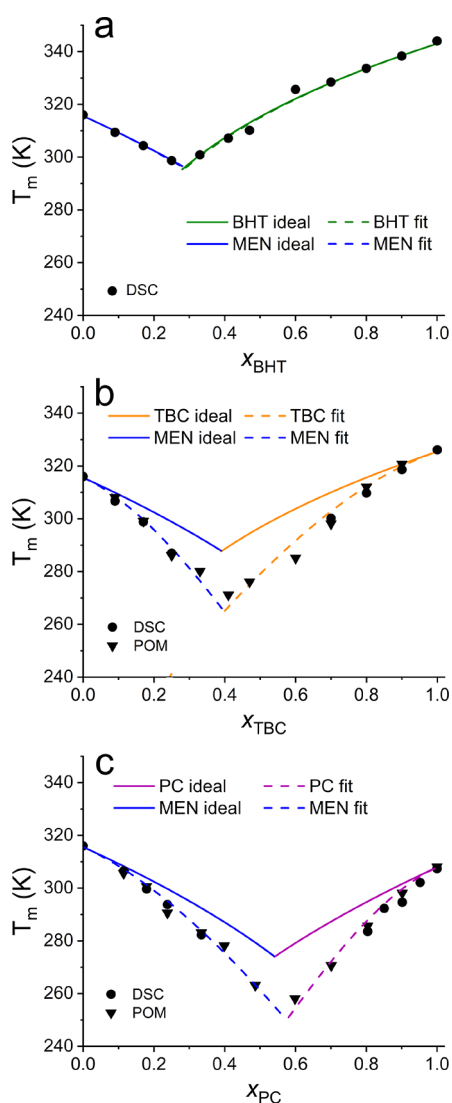
Figure 2. SLE phase diagrams for (a) BHT/MEN, (b) TBC/MEN, and (c) PC/MEN binary mixtures obtained from the experimental MP temperatures T_m determined by DSC and POM measurements (dashed curves), compared to the theoretical predictions for ideal mixtures (full curves).

Table 1. Molar Fraction x_i and MP Temperature T_m at the Eutectic Composition, Together with the Effective Interaction Parameter χ, for the BHT/MEN, TBC/MEN, and PC/MEN Binary Mixtures Determined from the Ideal and Best-Fit SLE Phase Diagrams Shown in Figure 2

	ideal		fit		
system	$x_{\text{BHT/TBC/PC}}$	T_m (K)	$x_{\text{BHT/TBC/PC}}$	T_m (K)	χ
BHT/MEN	0.29	295.5	0.29	295.6	−0.1(1)
TBC/MEN	0.39	287.8	0.39	264.9	−2.6(3)
PC/MEN	0.54	274.0	0.57	249.9	−2.5(2)

value obtained after interpolation of the experimental melting temperatures is 295.6 K and thus almost matches the ideal one (Table 1). A behavior close to thermal ideality is observed for the whole composition range, as the obtained MPs are found to lie close to the ideal phase diagram (Figure 2a). This result, alongside the determined χ values, which are close to zero (Table 1), suggests that the intermolecular BHT−MEN

interactions with respect to the precursor states are not favorable enough to provide a DES. A different situation is observed for the TBC/MEN and PC/MEN systems (Figure 2b and c, respectively). At the intermediate mixture compositions, DSC experiments revealed no melting during the heating scans due to a lack of crystallization in the cooling stage, already suggesting stronger interactions between the parent compounds. Therefore, the MPs of these mixtures were determined by using the POM technique. In the TBC/MEN system, a progressive deviation from ideality is observed and maximized close to the eutectic composition (Figure 2b). Although the ideal and experimental eutectic points are both located at $x_{\text{TBC}} = 0.39$, the experimental MP at the eutectic composition is well below the expected value, showing an MP depression of 22.9 K (Table 1). A similar behavior is shown by the PC/MEN mixtures (Figure 2c), where the deviation from ideality is a maximum for the eutectic composition at $x_{\text{PC}} = 0.57$, for which an MP of 249.9 K is obtained, while the predicted one of 274.0 K at $x_{\text{PC}} = 0.54$ delivers an MP depression of 24.1 K. In conclusion, the BHT/MEN system can be classified as an ideal eutectic solvent, while the TBC/MEN and PC/MEN mixtures behave as type V DESs. Note that, differently from the BHT/MEN case, the χ parameters determined for the TBC/MEN and PC/MEN systems show negative values (Table 1), suggesting that the higher attractive interaction between the precursor compounds could be the main factor leading to the classification of these systems as type V DESs.

Raman Spectroscopy Results. The sensitivity of the Raman spectroscopy toward the O−H vibration has been exploited to retrieve information on the H-bonding aggregation in the BHT/MEN, TBC/MEN, and PC/MEN mixtures. In Figure 3, we report the magnified ν_{OH} contribution of the spectra recorded in the 3100−3800 cm^{-1} range, while the complete Raman profiles are shown in Figure S1. The ν_{OH} signal of pristine MEN is dominated by a broad band centered at about 3400 cm^{-1} (Figure 3a−c). This low-frequency contribution has been previously associated with hydroxyls behaving as H-bond donors by means of the hydrogen atom, while contemporaneously employing the oxygen atom as a H-bond receptor through its lone pairs, and labeled as δ-OHs.[33,57−63] This spectral evidence therefore indicates the formation of H-bonded networks or aggregates and a high extent of self-association of the MEN molecules in the precursor compound. BHT addition to MEN (Figure 3a) is translated into the enhancement of a high-frequency contribution appearing in the 3600−3650 cm^{-1} region, up to the formation of a distinct narrow peak with a maximum at 3647 cm^{-1} for the BHT n-heptane solution. This feature has been previously connected with "free" hydroxyl groups not involved in H-bonding and labeled as α-OH.[57−59,64,65] Note that β-OH also resonate in the same spectral region and are referred to hydroxyls behaving as proton acceptors with the oxygen atom, while contemporaneously not behaving as H-bond donors with the hydrogen atom. A pictorial representation of these hydroxyl types is given in Figure 3d. In both cases, the hydrogen atom is free from H-bonding, resulting in a similar frequency of the O−H oscillator.[59] It is worth noting that such a spectral evolution occurs at the expense of the δ-OH band characterizing the pristine MEN, which is sequentially blue-shifted and flattened for increasing BHT concentration (Figure 3a). Altogether these findings suggest that the addition of the sterically hindered BHT to MEN is
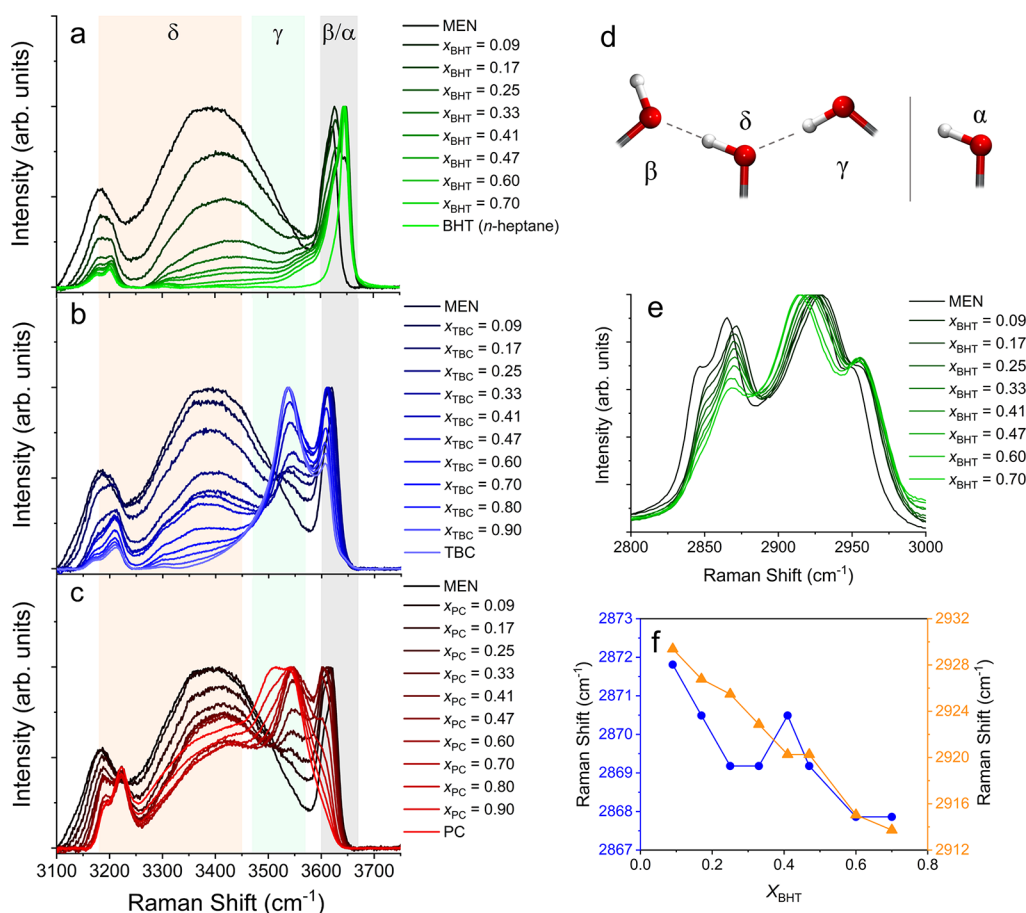
Figure 3. Raman spectra normalized for the maximum absorption in the ν_{OH} region of the (a) BHT/MEN, (b) TBC/MEN, and (c) PC/MEN mixtures at different molar fractions of the components and of the BHT (n-heptane solution), TBC, PC, and MEN compounds at 323 K. The spectral ranges corresponding to the α/β-, γ-, and δ-OH contributions according to literature data[57−59,65] are highlighted on the background, and their pictorial representation is given in panel d. (e) Raman spectra normalized for the maximum absorption in the C−H stretching region of the BHT/MEN mixtures at different molar fractions of the components at 323 K and (f) corresponding values of the two peak maxima reported in the function of x_{BHT}.

able to perturb the H-bonded association present in the pristine compound and to promote an increasing isolation of the BHT and MEN molecules in terms of H-bonding. As a consequence, the hindering effect provided by the two *tert*-butyl substituents is highly detrimental for the establishment of H-bond interactions by the BHT component.

A similar flattening of the ~3400 cm^{-1} band characterizing pristine MEN is also evident upon addition of the sterically semifree TBC compound (Figure 3b). However, at variance with the BHT/MEN case, this spectral evolution occurs alongside the enhancement of a marked peak appearing at ~3540 cm^{-1}. This contribution lies in the middle of the spectral region connected with γ-OHs, representing terminal proton-donating hydroxyls with the lone pairs of the oxygen atom not involved in H-bonding (Figure 3d), being thus responsible for the formation of H-bonded dimers.[57,58,65] Note that the phenolic nature of TBC makes its hydroxyl group more positive due to resonance effects and the hydrogen atom a better donor, while the oxygen atom becomes a worse acceptor (Figure S2b). On the other hand, MEN possesses no aromaticity, so that the TBC-MEN donor−receptor inter-action should be the most favored one at least from an electrostatic point of view. This also applies for BHT (Figure S2a), but the steric exclusion in both the *ortho*-positions of the hydroxyl group is evidently able to overwhelm this favorable

electronic effect. Conversely, the TBC molecule carries only one *tert*-butyl substituent, thus leaving partial access to the hydroxyl group and allowing the establishment of the favorable TBC−MEN interaction. The obtained Raman profiles are therefore compatible with the replacement of the H-bonded aggregates among MEN molecules through the formation of TBC-MEN dimers due to the competition of the more acidic TBC proton.

The Raman spectrum of the sterically free PC compound also consists of a marked γ-OH contribution, plus a δ-OH one similar to that characterizing pristine MEN (Figure 3c). This fingerprint indicates that the molecular association in the precursor compound consists of both H-bonded agglomerates among PC molecules and PC−PC donor−acceptor dimers. Once PC is mixed with MEN, a retention of both the γ- and δ-OH contributions is observed for all of the explored compositions. As in the case of the sterically semifree TBC, also the PC species has better H-bond donor and worse receptor capability due to its phenolic nature (Figure S2c). However, in the PC molecule, there are no substituents in the *ortho*-positions with respect to the hydroxyl group, allowing this molecule to intercalate in H-bonded networks and behave simultaneously as a H-bond donor and receptor.

The establishment of the TBC-MEN and PC-MEN donor−receptor H-bonds, as evidenced by the Raman experimental
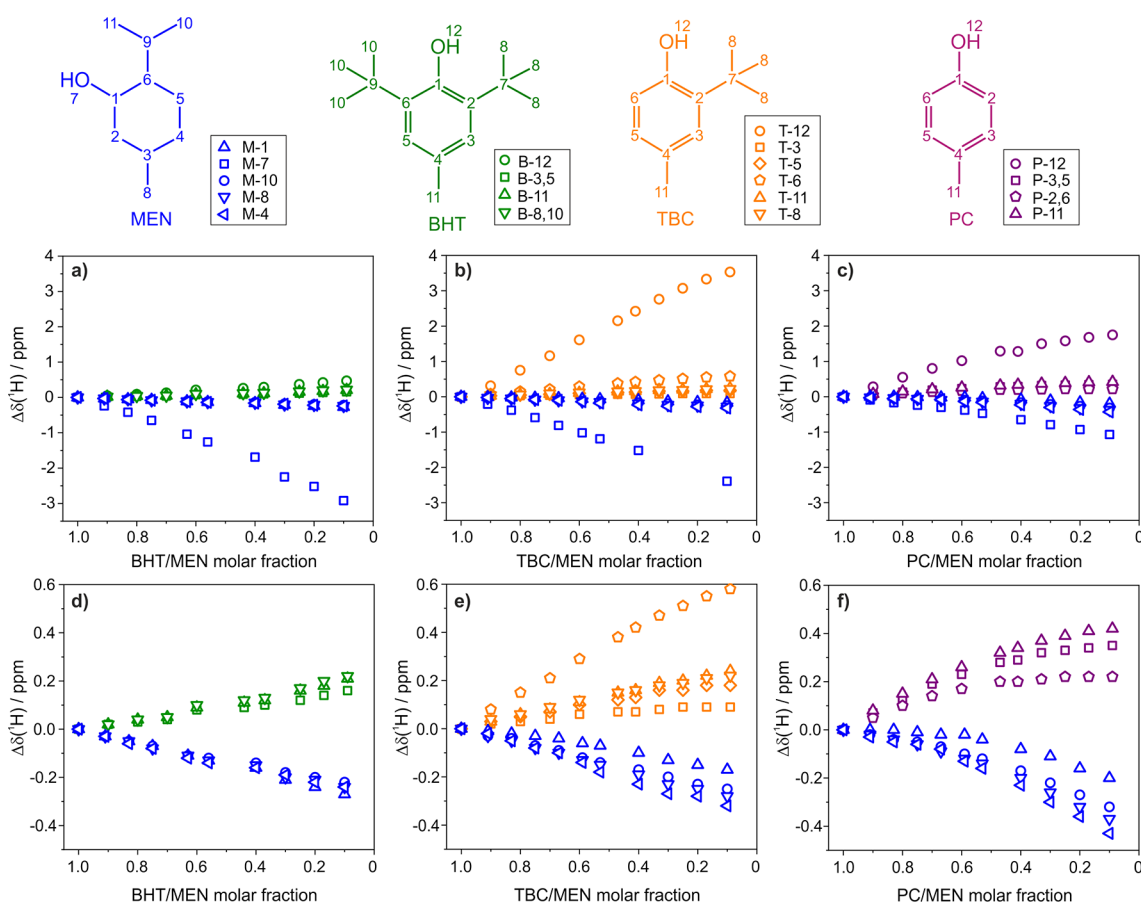
Figure 4. Change in ^{1}H NMR chemical shift of selected protons $\Delta\delta_H$ of BHT (green), TBC (orange), PC (purple), and MEN (blue) in the (a,d) BHT/MEN, (b,e) TBC/MEN, and (c,f) PC/MEN mixtures as a function of composition at 343 K. For each component (MEN, BHT, TBC, PC), $\Delta\delta_H$ is defined as the chemical shift difference of each signal in the mixture (BHT/MEN, TBC/MEN, PC/MEN) and in the neat component. A molar fraction of 1.0 corresponds then to the pure individual component.

outcomes (Figure 3b,c), should in principle allow the strongest interplay between the parent compounds and be the main driving force leading to the behavior of the TBC/MEN and PC/MEN systems as type V DESs (Figure 2b,c). As concerns the BHT/MEN mixtures, the poor participation of the BHT molecules to H-bonding (Figure 3a) can explain the ideal thermal behavior of this eutectic (Figure 2a). Nevertheless, a liquid phase is obtained at room temperature for compositions close to the eutectic one, and at the $x_{BHT} = 0.25$ molar fraction this mixture has been previously employed under room temperature operative conditions,[34−36] suggesting that some sort of interplay must occur upon mixing of the parent compounds. To deepen this aspect and check if additional interactions are present, we inspected the spectral region associated with the C−H stretching modes in the Raman profiles of the BHT/MEN mixtures (see Figure 3e). The wavenumber region between 2800 and 3000 cm^{-1} comprises a complex set of overlapped peaks due to the symmetric and antisymmetric CH$_2$ and CH$_3$ stretching,[66−68] which can be associated with the *tert*-butyl, isopropyl, and methyl substituents of the BHT and MEN components. Nevertheless, the entire group of C−H vibrations is found to shift at lower wavenumbers upon BHT addition to MEN. This effect can be better appreciated from the positions of the two main peak maxima reported as a function of the BHT concentration in Figure 3f. A decrease of the C−H stretching frequency has been previously invoked as an indicator for the increase of the

alkyl chain interactions and conformational order.[66,67] This result is compatible with the establishment of apolar−apolar attractions among the alkyl substituents of the BHT and MEN components, suggesting that this may be also a driving force for the BHT/MEN eutectic formation. As such dispersion forces are known to be weak, the experimentally determined MP results are close to the ideality, and this system is classified as an ideal eutectic. Note that a systematic shift of the C−H stretching bands frequency is observed also upon MEN mixing with TBC and PC (Figure S3a and b, respectively), even if of a smaller extent with respect to the BHT/MEN case. This evidence suggests that apolar−apolar attractions could also play a role in the TBC/MEN and PC/MEN mixtures, even if the H-bonding contribution in these systems is overwhelming with respect to these interactions.

NMR Characterization. The ^{1}H NMR spectra collected on the BHT/MEN, TBC/MEN, and PC/MEN mixtures are reported in Figure S4, while in Figure 4 we present the change in the chemical shift of selected protons ($\Delta\delta_H = \delta_{mixture} - \delta_{neat}$) of the constituents across the full composition range with respect to their pure state.[33] A rise in δ_H (downfield shift) is indicative of protons in a less shielded magnetic environment, thus as far as the hydroxyl protons are concerned this descriptor delivers information on the extent of H-bonding formation, since an increase in this interaction is expected to lower the electron density and make the nucleus less shielded with respect to the magnetic field.[69] Therefore, a downfield

shift of the OH signal ($\Delta\delta_{OH} > 0$) has to be interpreted here as due to the formation of H-bonds in the mixture that are stronger than the existing ones in the neat compounds. Similarly, a low-frequency (upfield) shift ($\Delta\delta_{OH} < 0$) indicates the weakening of H-bonds in the pure component and their replacement with relatively less strong H-bonds in the mixture.[23,70−72] Concerning the BHT/MEN system, the gradual addition of BHT to MEN is translated into a marked upfield shift of the MEN hydroxyl proton chemical shift (Figure S4), with $\Delta\delta_{MEN-OH}$ reaching a value of −2.9 ppm for the highest BHT concentration (Figure 4a). This behavior can be attributed to a weakening of the H-bond interactions among the MEN molecules with respect to the pristine compound. On the other hand, this evolution is not mirrored by an equal downfield shift of the δ_H of the BHT hydroxyl proton (Figure S4), showing very low $\Delta\delta_{BHT-OH}$ values through the full composition range (Figure 4a). The whole result therefore indicates that the progressive breaking of the MEN−MEN intermolecular association provoked by the addition of the sterically hindered BHT is not compensated by a significant establishment of further H-bonds, confirming the increasing isolation of the two compounds in terms of H-bonding in agreement with the Raman spectroscopy results (Figure 3a).

A different situation is obtained for the TBC/MEN system (Figure 4b). Here, the addition of the sterically semifree TBC to MEN provokes a decrease of the MEN hydroxyl $\Delta\delta_H$ of a similar extent to what is found for the BHT/MEN mixtures ($\Delta\delta_{MEN-OH}$ = −2.4 ppm for the highest TBC concentration). However, such an evolution goes hand in hand with a marked increase of the $\Delta\delta_H$ of the TBC hydroxyl proton, with $\Delta\delta_{TBC-OH}$ reaching a value of 3.5 ppm for the highest MEN concentration. This finding indicates that the breaking of the H-bonded agglomerates initially present in pristine MEN is accompanied by a strengthening of the H-bonds played by the TBC molecules with respect to the precursor state. This massive change can be explained with the strong H-bond donor and poor receptor capabilities of the TBC species due to resonance effects (Figure S2b). Indeed, when mixed with MEN, the TBC molecules encounter a "regular" H-bond acceptor with no mesomeric effects, so that the preferential TBC-MEN interaction is established, which according to the Raman spectroscopy results is mostly played through TBC-MEN H-bonded dimers (Figure 3b). Such a concept has been previously indicated as "polarity asymmetry" and used to explain the MP depression in the archetypal type V DES formed by thymol and MEN.[16,33] However, in the case of TBC, this molecule adds to the polarity asymmetry also the steric effect, as the *tert*-butyl substituent in the *ortho*-position to the hydroxyl group is a further factor preventing contemporaneous behavior as a H-bond donor and acceptor. This exasperated asymmetry leads to poor H-bond interactions in the precursor state, where only TBC molecules are present, and explains the marked increase in the $\Delta\delta_H$ of the TBC hydroxyl proton upon MEN addition (Figure 4b) and ultimately the deviation from thermal ideality of the TBC/MEN system (Figure 2b).

Addition of the sterically free PC to MEN also provokes a decrease of the $\Delta\delta_H$ of the MEN hydroxyl proton (Figure 4c), even if to a lower extent with respect to the BHT/MEN and TBC/MEN cases ($\Delta\delta_{MEN-OH}$ = −1.1 ppm for the highest PC concentration). This provides evidence that the H-bonded network of pristine MEN is less perturbed by the PC introduction as compared to the BHT and TBC ones. Such

evolution is accompanied by an increase of the $\Delta\delta_H$ of the PC hydroxyl, which is greater than that obtained for BHT (Figure 4a) but lower than the TBC one (Figure 4b). As for TBC, PC is also phenolic in nature and thus a stronger H-bond donor and weaker receptor (Figure S2c). However, in this case, there is no steric hindrance in the *ortho*-positions to the hydroxyl group, so that the H-bond donor/receptor asymmetry only relies on electronic effects. For this reason, the intermolecular aggregation in the precursor is less prevented than in the TBC case, and H-bonded agglomerates among PC molecules are also present, as evidenced by the δ-OH contribution in the Raman profile of the pristine compound (Figure 3c). When mixed with MEN, the PC-MEN donor−receptor H-bond is in any case established as the most favored interaction, leading to a significant increase of the $\Delta\delta_H$ of the PC hydroxyl proton (Figure 4c) and the achievement of a type V DES (Figure 2c), but the changes felt by the PC molecule with respect to the initial state are less pronounced as compared to the TBC case.

Despite a less intuitive interpretation, chemical shift variations at the other proton sites can give further insights into the evolution of the intermolecular network of the mixtures. When looking at selected protons of MEN in the TBC/MEN and PC/MEN mixtures (Figure 4e,f), the situation resembles that already observed in the type V DES formed by thymol and MEN;[33] i.e., the proton in the *para*-position to the hydroxyl group (M-4) exhibits the second greatest shift, followed by methyl protons M-8 and M-10, while the closest proton to the hydroxyl group (M-1) shows the smallest $\Delta\delta_H$. This indicates that additional dispersive interactions involving MEN molecules are strengthened with respect to neat MEN upon TBC/PC addition. However, while the behavior of TBC is very close to that of thymol, with a significant $\Delta\delta_H$ recorded for the nearest proton to the OH group (T-6), PC displays the largest $\Delta\delta_H$ for the methyl protons P-11 and the smallest shift for the protons in the *ortho*-position to the hydroxyl group (P-2,6). This supports a scenario where the intermolecular network in the pure sterically free PC when mixed with MEN is less perturbed in terms of H-bonds and more affected in terms of dispersive forces with respect to the sterically semifree TBC. The situation in the BHT/MEN system is very different, with only minor and clustered shifts observed at all proton sites of both components (Figure 4d), and the second largest $\Delta\delta_H$ is observed for M-1 and B-8,10. This confirms that, when mixing MEN with the sterically hindered BHT, the most drastic change is the weakening of MEN−MEN H-bonds, which is not compensated by the establishment of other stabilizing interactions of similar strength.

MD Simulations Results. To obtain an atomistic description of the structural arrangement among the different components, we carried out MD simulations of the BHT/MEN, TBC/MEN, and PC/MEN mixtures. Classical MD simulations have been performed on systems covering the full composition range between the parent compounds, in analogy with the experimental measurements. However, this level of theory was insufficient for the description of these systems, and in particular it delivered a biased behavior of the TBC molecule establishing an intramolecular interaction between the hydroxyl proton and the *tert*-butyl group, thus not behaving as a H-bond donor in contradiction with the experimental Raman (Figure 3b) and NMR (Figure 4b) spectroscopy outcomes. Further discussion about the classical MD results is referred to the SI. Here, we present the results of the DFTB-MD simulations, which we performed on the BHT/
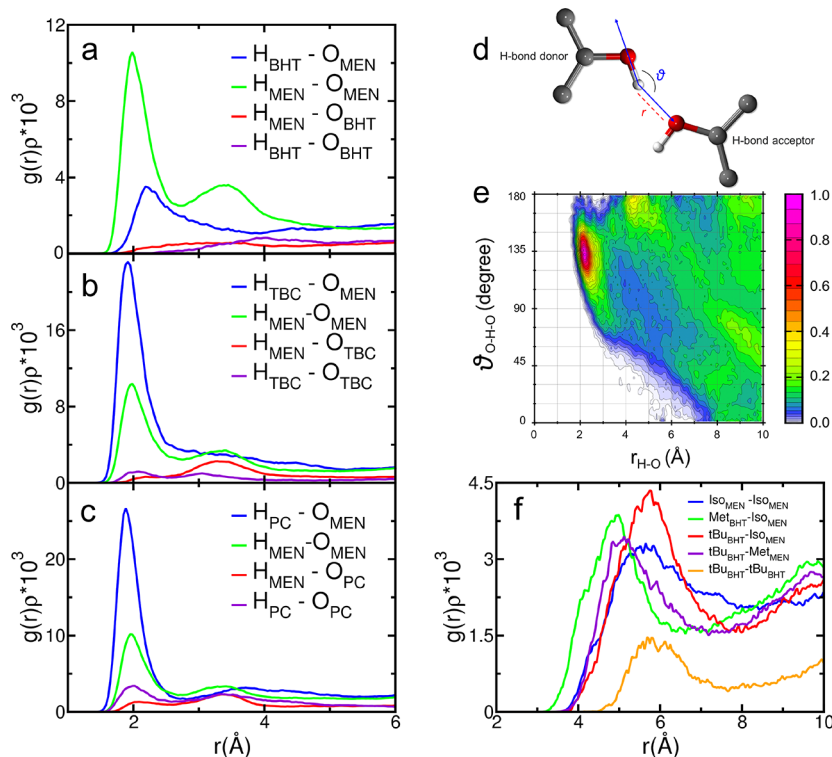
Figure 5. Radial distribution functions multiplied by the numerical densities of the observed atoms, $g(r)\rho$'s, for the intermolecular H−O distributions calculated from the DFTB-MD simulations at 298 K of the (a) BHT/MEN, (b) TBC/MEN, and (c) PC/MEN systems at $x_{BHT/TBC/PC}$ = 0.25 composition. The atom names are employed according to the nomenclature reported in Figure 1. Reference system (d) and CDF (e) between the $H_{BHT}−O_{MEN}$ $g(r)$ and angular distribution function computed from the DFTB-MD simulation of the BHT/MEN system. The color box on the right side is relative to the probability function of finding the inspected particle at that distance and angle normalized to one. (f) $g(r)\rho$'s between the COMs of the alkyl functional groups of the components computed from the DFTB-MD simulation of the BHT/MEN system (Iso = isopropyl, Met = methyl, tBu = *tert*-butyl).

MEN, TBC/MEN, and PC/MEN mixtures for the $x_{BHT/TBC/PC}$ = 0.25 composition. The x_{BHT} = 0.25 sample is the closest to the eutectic point for the BHT/MEN system and has been previously employed for application purposes,[34,35] while for the TBC/MEN and PC/MEN ones, we decided to study the same composition for the sake of comparison among the three eutectics. Site−site radial distribution functions $g(r)$'s have been calculated for all of the possible intermolecolar H−O distributions between the hydroxyl groups of the components to obtain insights into the established H-bond interactions. The obtained $g(r)$'s are shown in Figure 5a−c, while in Table 2 we list the maximum positions of the first peak and the coordination numbers N computed integrating each curve up to a cutoff distance chosen at the first minimum. As can be observed, in the BHT/MEN system, the $H_{MEN}−O_{MEN}$ $g(r)$ associated with the H bonds among MEN molecules is overwhelming with respect to the others (Figure 5a). The maximum distance of 1.98 Å is in line with those typically observed for strong H bonds,[18−22,36,73] while the obtained integration number is 0.34 (Table 2). Conversely, the $g(r)$'s where the sterically hindered BHT molecule behaves as a H-bond acceptor, namely, the $H_{MEN}−O_{BHT}$ and $H_{BHT}−O_{BHT}$ ones, do not show distinguishable peaks, confirming the hampered access to the hydroxyl group of this component. A special comment must be dedicated to the $H_{BHT}−O_{MEN}$ distribution. Here, a distinct peak is obtained, suggesting that BHT behaves as a H-bond donor toward the MEN molecule. However, careful inspection of this $g(r)$ reveals that the maximum position is 2.18 Å (Table 2), thus relatively longer

than a strong H bond. Provided that the bond distance is not the only criterion to define the H-bond strength,[73] we carried out the analysis of the bond angle formed between the H-bond donor and acceptor sites, which we correlated with the $H_{BHT}−O_{MEN}$ $g(r)$ in a combined distribution function (CDF). The reference system for this analysis is depicted in Figure 5d, while the obtained CDF is shown in Figure 5e. Here, a high probability spot is located around an angle value of about 135°, thus far away from the 180° angle usually associated with strong H-bonds.[36,73] This result suggests that the BHT molecule may tentatively behave as a H-bond donor toward the MEN molecules due to its phenolic nature, but the steric encumbrance around its hydroxyl group prevents this species from establishing a significant H-bond interaction. Since no relevant H-bonds are found among the components of this system, we also computed the $g(r)$'s between the centers of mass (COMs) of the alkyl substituents to get confirmation about interactions among the hydrophobic moieties suggested by the Raman experimental outcomes (Figure 3e,f). As shown in Figure 5f, all of the obtained curves present well-defined first peaks displaying a remarkable degree of structuration. This evidence subtends a high degree of structural order among the alkyl chains and pleads for apolar−apolar attractions as a driving force for the BHT/MEN eutectic formation.

Concerning the TBC/MEN system, the more relevant distribution is the $H_{TBC}−O_{MEN}$ one (Figure 5b), which shows a remarkably short distance of 1.92 Å and an N value of 0.68 (Table 2). This $g(r)$ is connected with the TBC-MEN donor−receptor H bond and confirms this interaction as the favored

Table 2. Structural Parameters of the $g(r)\rho$'s for the Intermolecular H−O Distributions Calculated from the DFTB-MD Simulations at 298 K of the BHT/MEN, TBC/ MEN, and PC/MEN Systems at $x_{BHT/TBC/PC} = 0.25$ Composition (Figure 5a−c) and from the DFTB-MD Simulations at 348 K of the BHT, TBC, PC, and MEN Compounds (Figure 6a)[a]

system	$g(r)$	r_{max} (Å)	N	cutoff (Å)
BHT/MEN	$H_{BHT}-O_{MEN}$	2.18	0.35	3.82
	$H_{MEN}-O_{MEN}$	1.98	0.34	2.72
	$H_{MEN}-O_{BHT}$			
	$H_{BHT}-O_{BHT}$			
TBC/MEN	$H_{TBC}-O_{MEN}$	1.92	0.68	2.82
	$H_{MEN}-O_{MEN}$	1.98	0.33	2.72
	$H_{MEN}-O_{TBC}$			
	$H_{TBC}-O_{TBC}$			
PC/MEN	$H_{PC}-O_{MEN}$	1.88	0.61	2.82
	$H_{MEN}-O_{MEN}$	1.95	0.31	2.72
	$H_{MEN}-O_{PC}$			
	$H_{PC}-O_{PC}$	2.02	0.12	2.58
BHT	$H_{BHT}-O_{BHT}$			
TBC	$H_{TBC}-O_{TBC}$			
PC	$H_{PC}-O_{PC}$	2.02	0.22	2.70
MEN	$H_{MEN}-O_{MEN}$	2.04	0.37	2.70

[a]r_{max} is the position of the first peak maximum, and N is the integration number calculated by integrating each curve up to the reported cutoff distance. The atom names are employed according to the nomenclature reported in Figure 1. No data are reported for the $g(r)\rho$'s that showed negligible peaks.

one in this mixture, followed by the $H_{MEN}-O_{MEN}$ $g(r)$ describing the self-aggregation among MEN molecules that is found to persist at this composition (Figure 5b). Differently, almost no peak is obtained for the $H_{MEN}-O_{TBC}$ distribution as this interaction is unfavored for electronic reasons, while the $H_{TBC}-O_{TBC}$ $g(r)$ is also negligible, confirming the hampered self-association among TBC molecules as due to both electronic and steric factors. A similar picture is obtained for the PC/MEN system, where the most relevant interaction is the $H_{PC}-O_{MEN}$ one, followed by the $H_{MEN}-O_{MEN}$ distribution (Figure 5c). However, here it is worth noticing that the $H_{PC}-O_{PC}$ distribution reflecting self-aggregation among PC molecules is slightly more marked than the correspondent $H_{TBC}-O_{TBC}$ one in the TBC/MEN system (Figure 5b), providing a potential confirmation about the higher tendency of the sterically free PC to self-interact.

To better unveil these issues, we also performed DFTB-MD simulations of the pristine compounds BHT, TBC, PC, and MEN. The intermolecular H−O $g(r)$'s describing the interaction among the precursor molecules in their pure states are shown in Figure 6a, while the correspondent parameters are listed in Table 2. As expected, the $H_{PC}-O_{PC}$ distribution shows a distinct first peak with a maximum at 2.02 Å, validating the self-association among the sterically free PC molecules in the pristine compound, and the same is true for the $H_{MEN}-O_{MEN}$ one in pristine MEN. The $H_{BHT}-O_{BHT}$ $g(r)$ shows no peak at all, confirming the hampered aggregation among the sterically hindered BHT molecules also in the precursor state. A special look is deserved for the $H_{TBC}-O_{TBC}$ distribution obtained for the sterically semifree TBC. Here, this function describing the H bond among TBC molecules does not show a distinct peak and seems to confirm the hampered self-
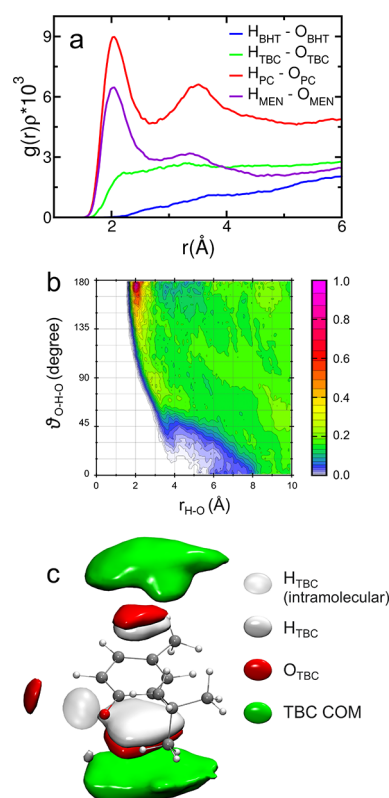

Figure 6. (a) Radial distribution functions multiplied by the numerical densities of the observed atoms, $g(r)\rho$'s, for the intermolecular H−O distributions calculated from the DFTB-MD simulations at 348 K of the BHT, TBC, PC, and MEN compounds. The atom names are employed according to the nomenclature reported in Figure 1. (b) CDF between the $H_{TBC}-O_{TBC}$ $g(r)$ and angular distribution function computed from the DFTB-MD simulation of the TBC compound. The color box on the right side is relative to the probability function of finding the inspected particle at that distance and angle normalized to one. (c) SDFs around the TBC molecule computed from the DFTB-MD simulation of the TBC compound. The functions have been computed with respect to an internal reference system that is integral to the carbon ring. The observed species are shown according to the color code reported on the right. The hydroxyl hydrogen atom of the reference molecule is represented by an intramolecular SDF. Isosurfaces have been drawn with the same density/maximum density ratio according to the following isovalues in nm^{-3}: H_{TBC} (6.4), O_{TBC} (7.0), TBC COM (7.6).

aggregation of the TBC precursor. A more detailed analysis has been achieved by calculating the CDF between this $g(r)$ and the angle distribution between the donor and acceptor sites, with the same reference system shown in Figure 5d. The obtained CDF displays a high intensity region around the ~180° value, which is consistent with a H-bond interaction (Figure 6b),[36,73] but a broad distribution is found also at other angle values. For the sake of comparison, the analogous CDFs computed for the H-bond networking PC and MEN compounds are shown in Figure S5. Here, probability spots are highly localized around the ~180° angle and are compatible with strong H-bond interactions. Further insights into the three-dimensional arrangement among TBC molecules in the pristine compound have been obtained by means of a spatial distribution function (SDF) calculations (Figure 6c). Here, the three-dimensional density distribution of the TBC hydroxyl hydrogen and oxygen atoms, as well as

molecular COM, has been computed around each TBC molecule taken as a reference. The first feature capturing the attention is that most of the observed probability spots are found close to the carbon body of the TBC reference, while only a small volume corresponding to the observed O_{TBC} atom is found close to the H_{TBC} reference one. This result, together with the poorly structured $H_{TBC}-O_{TBC}$ $g(r)$ (Figure 6a) and with the correspondent CDF (Figure 6b), confirms that the TBC−TBC H-bond interaction in the pristine compound is likely to be tentatively formed, but the contemporaneous behavior of TBC as a H-bond donor/receptor is hampered because of a combined effect between the unfavorable electronic and steric factors. This picture is in agreement with the body of evidence provided by the experimental outcomes and serves as a rationalization of the thermal behavior of the TBC/MEN system in relation with the BHT/MEN and PC/MEN ones.

CONCLUSIONS

A detailed study of the BHT/MEN, TBC/MEN, and PC/MEN mixtures has been carried out with the aim of enlightening the various contributions ruling the intermolecular interactions among the components and the eutectic formation. The thermal characterization showed that the BHT/MEN system can be classified as an ideal eutectic, while the TBC/MEN and PC/MEN mixtures behave as type V DES for a wide range of compositions around the eutectic point. Addition of the sterically hindered BHT to MEN is detrimental toward the H-bonded agglomerates among MEN molecules present in the pristine compound, which are not compensated by the establishment of further H-bond interactions. Nevertheless, a liquid phase at room temperature is obtained for compositions close to the eutectic one. In the absence of relevant H-bonding, the high structural order observed among the alkyl functional groups of the BHT and MEN constituents subtends for apolar−apolar attractions as a driving force of the eutectic formation. Addition of the sterically semifree TBC to MEN also provokes the breaking of the H-bonded network of the pristine compound, but in this case it is replaced by the formation of the more favorable TBC-MEN donor−receptor H-bonds. This behavior derives from a concurrence of electronic and steric factors, as the better H-bond donor and worse receptor capabilities of the TBC molecule due to mesomeric effects are exasperated by the presence of one *tert*-butyl group in *ortho*-position to the hydroxyl. The whole effect is that of making the intermolecular interactions in the TBC/MEN mixtures much more favorable than in the precursor TBC compound, and a type V DES is obtained as a result. The sterically free PC molecule is also a better H-bond donor and worse receptor due to a phenolic nature, but, differently from the TBC case, a considerable amount of self-association is observed already in the precursor compound by means of both PC−PC donor−receptor dimers and H-bonded networks. This behavior is maintained also upon mixing with MEN, but the PC-MEN donor−receptor H-bond is established as a more favorable interaction, and this is the driving force for the type V DES formation. Evidence for apolar−apolar attractions among the components are also found for the TBC/MEN and PC/MEN mixtures, but they play a marginal role compared to the dominating H-bond contribution. The body of evidence that we obtained here was therefore able to clarify the different factors on the molecular level influencing the thermal behavior of the studied eutectic mixtures. Along with the peculiarity of the inspected systems, the impact of this work is that of providing new tools for a more conscious understanding of the complex correlations between local structure and macroscopic properties in hydrophobic DESs.

ASSOCIATED CONTENT

Ⓢᴵ Supporting Information

The Supporting Information is available free of charge at https://pubs.acs.org/doi/10.1021/acssuschemeng.3c01209.

> List of the prepared samples, details about the building of the SLE phase diagrams, details of the simulated MD systems, Raman and NMR spectroscopy additional results, discussion of classical MD results (PDF)

AUTHOR INFORMATION

Corresponding Authors

Matteo Busato − *Department of Chemistry, University of Rome "La Sapienza", 00185 Rome, Italy;* ⓞ orcid.org/0000-0002-9450-0481; Email: matteo.busato@uniroma1.it

Paola D'Angelo − *Department of Chemistry, University of Rome "La Sapienza", 00185 Rome, Italy;* ⓞ orcid.org/0000-0001-5015-8410; Email: p.dangelo@uniroma1.it

Authors

Giorgia Mannucci − *Department of Chemistry, University of Rome "La Sapienza", 00185 Rome, Italy;* ⓞ orcid.org/0000-0002-6170-3522

Lorenzo Augusto Rocchi − *Department of Chemistry, University of Rome "La Sapienza", 00185 Rome, Italy;* ⓞ orcid.org/0000-0002-2565-5324

Maria Enrica Di Pietro − *Department of Chemistry, Materials and Chemical Engineering "G. Natta", Politecnico di Milano, 20133 Milan, Italy;* ⓞ orcid.org/0000-0002-2370-1948

Angela Capocefalo − *Institute for Complex Systems, National Research Council, 00185 Rome, Italy;* Present Address: Department of Physical and Chemical Sciences, University of L'Aquila, 67100 Coppito, L'Aquila, Italy; ⓞ orcid.org/0000-0001-7005-3309

Elisa Zorzi − *Department of Chemistry, University of Rome "La Sapienza", 00185 Rome, Italy*

Paolo Casu − *Department of Chemistry, University of Rome "La Sapienza", 00185 Rome, Italy*

Daniele Veclani − *Institute for Organic Synthesis and Photoreactivity, National Research Council, 40129 Bologna, Italy*

Franca Castiglione − *Department of Chemistry, Materials and Chemical Engineering "G. Natta", Politecnico di Milano, 20133 Milan, Italy;* ⓞ orcid.org/0000-0003-2413-8808

Andrea Mele − *Department of Chemistry, Materials and Chemical Engineering "G. Natta", Politecnico di Milano, 20133 Milan, Italy;* ⓞ orcid.org/0000-0002-0351-0538

Andrea Martinelli − *Department of Chemistry, University of Rome "La Sapienza", 00185 Rome, Italy;* ⓞ orcid.org/0000-0002-6401-9988

Paolo Postorino − *Department of Physics, University of Rome "La Sapienza", 00185 Rome, Italy;* ⓞ orcid.org/0000-0002-3809-0676

Complete contact information is available at:
https://pubs.acs.org/10.1021/acssuschemeng.3c01209

Notes

The authors declare no competing financial interest.

■ REFERENCES

(1) Francisco, M.; van den Bruinhorst, A.; Kroon, M. C. Low-Transition-Temperature Mixtures (LTTMs): A New Generation of Designer Solvents. *Angew. Chem., Int. Ed.* **2013**, *52*, 3074−3085.

(2) Smith, E. L.; Abbott, A. P.; Ryder, K. S. Deep Eutectic Solvents (DESs) and Their Applications. *Chem. Rev.* **2014**, *114*, 11060−11082.

(3) Hansen, B. B.; et al. Deep Eutectic Solvents: A Review of Fundamentals and Applications. *Chem. Rev.* **2021**, *121*, 1232−1285.

(4) Murakami, Y.; Das, S. K.; Himuro, Y.; Maeda, S. Triplet-sensitized Photon Upconversion in Deep Eutectic Solvents. *Phys. Chem. Chem. Phys.* **2017**, *19*, 30603−30615.

(5) Di Pietro, M. E.; Mele, A. Deep Eutectics and Analogues as Electrolytes in Batteries. *J. Mol. Liq.* **2021**, *338*, 116597.

(6) Abbott, A. P.; Capper, G.; Davies, D. L.; Rasheed, R. K.; Archer, J.; John, C. Electrodeposition of Chromium Black from Ionic Liquids. *Trans. Inst. Met. Finish.* **2004**, *82*, 14−17.

(7) Danilov, F. I.; Protsenko, V. S.; Kityk, A. A.; Shaiderov, D. A.; Vasil'eva, E. A.; Kumar, U. P.; Kennady, C. J. Electrodeposition of Nanocrystalline Nickel Coatings from a Deep Eutectic Solvent with Water Addition. *Prot. Met. Phys. Chem. Surf.* **2017**, *53*, 1131−1138.

(8) Ruesgas-Ramón, M.; Figueroa-Espinoza, M. C.; Durand, E. Application of Deep Eutectic Solvents (DES) for Phenolic Compounds Extraction: Overview, Challenges, and Opportunities. *J. Agric. Food Chem.* **2017**, *65*, 3591−3601.

(9) Yuan, Z.; Liu, H.; Yong, W. F.; She, Q.; Esteban, J. Status and Advances of Deep Eutectic Solvents for Metal Separation and Recovery. *Green Chem.* **2022**, *24*, 1895−1929.

(10) Zubeir, L. F.; van Osch, D. J. G. P.; Rocha, M. A. A.; Banat, F.; Kroon, M. C. Carbon Dioxide Solubilities in Decanoic Acid-Based Hydrophobic Deep Eutectic Solvents. *J. Chem. Eng. Data* **2018**, *63*, 913−919.

(11) Abbott, A. P.; Capper, G.; Davies, D. L.; Rasheed, R. K.; Tambyrajah, V. Quaternary Ammonium Zinc- or Tin-containing Ionic Liquids: Water Insensitive, Recyclable Catalysts for Diels−Alder Reactions. *Green Chem.* **2002**, *4*, 24−26.

(12) Abbott, A. P.; Bell, T. J.; Handa, S.; Stoddart, B. O-Acetylation of Cellulose and Monosaccharides Using a Zinc Based Ionic Liquid. *Green Chem.* **2005**, *7*, 705−707.

(13) Kang, L.; Jun, H.; McCall, J. Physicochemical Studies of Lidocaine−menthol Binary Systems for Enhanced Membrane Transport. *Int. J. Pharm.* **2000**, *206*, 35−42.

(14) Yong, C. S.; Jung, S. H.; Rhee, J.-D.; Choi, H.-G.; Lee, B.-J.; Kim, D.-C.; Choi, Y. W.; Kim, C.-K. Improved Solubility and In Vitro Dissolution of Ibuprofen from Poloxamer Gel Using Eutectic Mixture with Menthol. *Drug Deliv* **2003**, *10*, 179−183.

(15) Martins, M. A. R.; Pinho, S. P.; Coutinho, J. A. P. Insights into the Nature of Eutectic and Deep Eutectic Mixtures. *J. Solution Chem.* **2019**, *48*, 962−982.

(16) Abranches, D. O.; Coutinho, J. A. Type V Deep Eutectic Solvents: Design and Applications. *Curr. Opin. Green Sustain. Chem.* **2022**, *35*, 100612.

(17) Abbott, A. P.; Capper, G.; Davies, D. L.; Rasheed, R. K.; Tambyrajah, V. Novel Solvent Properties of Choline Chloride/Urea Mixtures. *Chem. Commun.* **2003**, 70−71.

(18) Di Pietro, M. E.; Hammond, O.; van den Bruinhorst, A.; Mannu, A.; Padua, A.; Mele, A.; Costa Gomes, M. Connecting Chloride Solvation with Hydration in Deep Eutectic Systems. *Phys. Chem. Chem. Phys.* **2021**, *23*, 107−111.

(19) Migliorati, V.; Sessa, F.; D'Angelo, P. Deep Eutectic Solvents: A Structural Point of View on the Role of the Cation. *Chem. Phys. Lett. X* **2019**, *737*, 100001.

(20) Busato, M.; Migliorati, V.; Del Giudice, A.; Di Lisio, V.; Tomai, P.; Gentili, A.; D'Angelo, P. Anatomy of a Deep Eutectic Solvent: Structural Properties of Choline Chloride:Sesamol 1:3 Compared to Reline. *Phys. Chem. Chem. Phys.* **2021**, *23*, 11746−11754.

(21) Busato, M.; Del Giudice, A.; Di Lisio, V.; Tomai, P.; Migliorati, V.; Gentili, A.; Martinelli, A.; D'Angelo, P. Fate of a Deep Eutectic Solvent upon Cosolvent Addition: Choline Chloride−Sesamol 1:3 Mixtures with Methanol. *ACS Sustain. Chem. Eng.* **2021**, *9*, 12252− 12261.

(22) Busato, M.; Di Lisio, V.; Del Giudice, A.; Tomai, P.; Migliorati, V.; Galantini, L.; Gentili, A.; Martinelli, A.; D'Angelo, P. Transition from Molecular- to Nano-scale Segregation in a Deep Eutectic Solvent - Water Mixture. *J. Mol. Liq.* **2021**, *331*, 115747.

(23) Di Pietro, M. E.; Tortora, M.; Bottari, C.; Colombo Dugoni, G.; Pivato, R. V.; Rossi, B.; Paolantoni, M.; Mele, A. In Competition for Water: Hydrated Choline Chloride:Urea vs Choline Acetate:Urea Deep Eutectic Solvents. *ACS Sust. Chem. Eng.* **2021**, *9*, 12262−12273.

(24) Busato, M.; Tofoni, A.; Mannucci, G.; Tavani, F.; Del Giudice, A.; Colella, A.; Giustini, M.; D'Angelo, P. On the Role of Water in the Formation of a Deep Eutectic Solvent Based on $NiCl_2 \cdot 6H_2O$ and Urea. *Inorg. Chem.* **2022**, *61*, 8843−8853.

(25) van Osch, D. J.; Zubeir, L. F.; van den Bruinhorst, A.; Rocha, M. A.; Kroon, M. C. Hydrophobic Deep Eutectic Solvents as Water-immiscible Extractants. *Green Chem.* **2015**, *17*, 4518−4521.

(26) Ribeiro, B. D.; Florindo, C.; Iff, L. C.; Coelho, M. A. Z.; Marrucho, I. M. Menthol-based Eutectic Mixtures: Hydrophobic Low Viscosity Solvents. *ACS Sustain. Chem. Eng.* **2015**, *3*, 2469−2477.

(27) van Osch, D. J. G. P.; Dietz, C. H. J. T.; Warrag, S. E. E.; Kroon, M. C. The Curious Case of Hydrophobic Deep Eutectic Solvents: A Story on the Discovery, Design, and Applications. *ACS Sustain. Chem. Eng.* **2020**, *8*, 10591−10612.

(28) Martins, M. A. R.; Silva, L. P.; Schaeffer, N.; Abranches, D. O.; Maximo, G. J.; Pinho, S. P.; Coutinho, J. A. P. Greener Terpene−Terpene Eutectic Mixtures as Hydrophobic Solvents. *ACS Sustain. Chem. Eng.* **2019**, *7*, 17414−17423.

(29) Abranches, D. O.; Martins, M. A. R.; Silva, L. P.; Schaeffer, N.; Pinho, S. P.; Coutinho, J. A. P. Phenolic Hydrogen Bond Donors in the Formation of Non-ionic Deep Eutectic Solvents: the Quest for Type V DES. *Chem. Commun.* **2019**, *55*, 10253−10256.

(30) Peloquin, A. J.; McCollum, J. M.; McMillen, C. D.; Pennington, W. T. Halogen Bonding in Dithiane/Iodofluorobenzene Mixtures: A New Class of Hydrophobic Deep Eutectic Solvents. *Angew. Chem., Int. Ed.* **2021**, *60*, 22983−22989.

(31) Hanada, T.; Goto, M. Synergistic Deep Eutectic Solvents for Lithium Extraction. *ACS Sustain. Chem. Eng.* **2021**, *9*, 2152−2160.

(32) Abranches, D. O.; Schaeffer, N.; Silva, L. P.; Martins, M. A. R.; Pinho, S. P.; Coutinho, J. A. P. The Role of Charge Transfer in the Formation of Type I Deep Eutectic Solvent-Analogous Ionic Liquid Mixtures. *Molecules* **2019**, *24*, 3687.

(33) Schaeffer, N.; Abranches, D. O.; Silva, L. P.; Martins, M. A.; Carvalho, P. J.; Russina, O.; Triolo, A.; Paccou, L.; Guinet, Y.; Hedoux, A.; Coutinho, J. A. Non-Ideality in Thymol + Menthol Type V Deep Eutectic Solvents. *ACS Sustain. Chem. Eng.* **2021**, *9*, 2203− 2211.

(34) Dal Bosco, C.; Di Lisio, V.; D'Angelo, P.; Gentili, A. Hydrophobic Eutectic Solvent with Antioxidant Properties: Application for the Dispersive Liquid−Liquid Microextraction of Fat-Soluble Micronutrients from Fruit Juices. *ACS Sustain. Chem. Eng.* **2021**, *9*, 8170−8178.

(35) Dal Bosco, C.; Mariani, F.; Gentili, A. Hydrophobic Eutectic Solvent-Based Dispersive Liquid-Liquid Microextraction Applied to the Analysis of Pesticides in Wine. *Molecules* **2022**, *27*, 908.

(36) Busato, M.; Mannucci, G.; Di Lisio, V.; Martinelli, A.; Del Giudice, A.; Tofoni, A.; Dal Bosco, C.; Migliorati, V.; Gentili, A.;

D'Angelo, P. Structural Study of a Eutectic Solvent Reveals Hydrophobic Segregation and Lack of Hydrogen Bonding between the Components. *ACS Sustain. Chem. Eng.* **2022**, *10*, 6337−6345.

(37) Mannucci, G.; Busato, M.; Tofoni, A.; D'Angelo, P. Structural Evolution of the Butylated Hydroxytoluene/Menthol Hydrophobic Eutectic Solvent Upon Methanol and Ethanol Cosolvent Addition. *J. Mol. Liq.* **2023**, *375*, 121302.

(38) Schaeffer, N.; Silva, L. P.; Coutinho, J. A. P. Comment on "Structural Study of a Eutectic Solvent Reveals Hydrophobic Segregation and Lack of Hydrogen Bonding between the Components. *ACS Sustain. Chem. Eng.* **2022**, *10*, 8669−8670.

(39) Busato, M.; Mannucci, G.; Di Lisio, V.; Martinelli, A.; Del Giudice, A.; Tofoni, A.; Dal Bosco, C.; Migliorati, V.; Gentili, A.; D'Angelo, P. Response to Comment on "Structural Study of a Eutectic Solvent Reveals Hydrophobic Segregation and Lack of Hydrogen Bonding between the Components. *ACS Sustain. Chem. Eng.* **2022**, *10*, 8671−8672.

(40) Glebov, A. L.; Mokhun, O.; Rapaport, A.; Vergnole, S.; Smirnov, V.; Glebov, L. B. *Vol. Bragg Gratings as Ultranarrow and Multiband Optical Filters*; Micro-Optics, 2012; pp 42−52, DOI: 10.1117/12.923575.

(41) Martínez, L.; Andrade, R.; Birgin, E. G.; Martínez, J. M. PACKMOL: A Package for Building Initial Configurations for Molecular Dynamics Simulations. *J. Comput. Chem.* **2009**, *30*, 2157−2164.

(42) Hess, B.; Bekker, H.; Berendsen, H. J. C.; Fraaije, J. G. E. M. LINCS: A Linear Constraint Solver for Molecular Simulations. *J. Comput. Chem.* **1997**, *18*, 1463−1472.

(43) Jorgensen, W. L.; Maxwell, D. S.; Tirado-Rives, J. Development and Testing of the OPLS All-Atom Force Field on Conformational Energetics and Properties of Organic Liquids. *J. Am. Chem. Soc.* **1996**, *118*, 11225−11236.

(44) Jasik, M.; Szefczyk, B. Parameterization and Optimization of the Menthol Force Field for Molecular Dynamics Simulations. *J. Mol. Model.* **2016**, *22*, 234.

(45) Darden, T.; York, D.; Pedersen, L. Particle Mesh Ewald: An Nlog(N) Method for Ewald Sums in Large Systems. *J. Chem. Phys.* **1993**, *98*, 10089−10092.

(46) Essmann, U.; Perera, L.; Berkowitz, M. L.; Darden, T.; Lee, H.; Pedersen, L. G. A Smooth Particle Mesh Ewald Method. *J. Chem. Phys.* **1995**, *103*, 8577−8593.

(47) Abraham, M. J.; Murtola, T.; Schulz, R.; Páll, S.; Smith, J. C.; Hess, B.; Lindahl, E. GROMACS: High Performance Molecular Simulations Through Multi-level Parallelism from Laptops to Supercomputers. *SoftwareX* **2015**, *1−2*, 19−25.

(48) Humphrey, W.; Dalke, A.; Schulten, K. VMD: Visual Molecular Dynamics. *J. Mol. Graph.* **1996**, *14*, 33−38.

(49) Brehm, M.; Kirchner, B. TRAVIS - A Free Analyzer and Visualizer for Monte Carlo and Molecular Dynamics Trajectories. *J. Chem. Inf. Model.* **2011**, *51*, 2007−2023.

(50) Hourahine, B.; et al. DFTB+, a Software Package for Efficient Approximate Density Functional Theory Based Atomistic Simulations. *J. Chem. Phys.* **2020**, *152*, 124101.

(51) Gaus, M.; Cui, Q.; Elstner, M. DFTB3: Extension of the Self-Consistent-Charge Density-Functional Tight-Binding Method (SCC-DFTB). *J. Chem. Theory and Comput.* **2011**, *7*, 931−948.

(52) Christensen, A. S.; Kubař, T.; Cui, Q.; Elstner, M. Semiempirical Quantum Mechanical Methods for Noncovalent Interactions for Chemical and Biochemical Applications. *Chem. Rev.* **2016**, *116*, 5301−5337.

(53) Christensen, A. S.; Elstner, M.; Cui, Q. Improving Intermolecular Interactions in DFTB3 Using Extended Polarization from Chemical-potential Equalization. *J. Chem. Phys.* **2015**, *143*, 084123.

(54) Gaus, M.; Goez, A.; Elstner, M. Parametrization and Benchmark of DFTB3 for Organic Molecules. *J. Chem. Theory Comput.* **2013**, *9*, 338−354.

(55) Addicoat, M. A.; Stefanovic, R.; Webber, G. B.; Atkin, R.; Page, A. J. Assessment of the Density Functional Tight Binding Method for Protic Ionic Liquids. *J. Chem. Theory Comput* **2014**, *10*, 4633−4643.

(56) Caldeweyher, E.; Ehlert, S.; Hansen, A.; Neugebauer, H.; Spicher, S.; Bannwarth, C.; Grimme, S. A Generally Applicable Atomic-charge Dependent London Dispersion Correction. *J. Chem. Phys.* **2019**, *150*, 154122.

(57) Lin-Vien, D.; Colthup, N. B.; Fateley, W. G.; Grasselli, J. G. In *The Handbook of Infrared and Raman Characteristic Frequencies of Organic Molecules*; Lin-Vien, D., Colthup, N. B., Fateley, W. G., Grasselli, J. G., Eds.; Academic Press: San Diego, 1991; pp 45−60, DOI: 10.1016/B978-0-08-057116-4.50010-9.

(58) Palombo, F.; Paolantoni, M.; Sassi, P.; Morresi, A.; Cataliotti, R. S. Spectroscopic Studies of the "Free" OH Stretching Bands in Liquid Alcohols. *J. Mol. Liq.* **2006**, *125*, 139−146.

(59) Paolantoni, M.; Sassi, P.; Morresi, A.; Cataliotti, R. S. Raman Noncoincidence Effect on OH Stretching Profiles in Liquid Alcohols. *J. Raman Spectrosc.* **2006**, *37*, 528−537.

(60) Böhmer, R.; Gainaru, C.; Richert, R. Structure and Dynamics of Monohydroxy Alcohols—Milestones Towards their Microscopic Understanding, 100 Years After Debye. *Phys. Rep.* **2014**, *545*, 125−195.

(61) Cabaço, M. I.; Besnard, M.; Cruz, C.; Morgado, P.; Silva, G. M. C.; Filipe, E. J. M.; Coutinho, J. A. P.; Danten, Y. Breaking the Structure of Liquid Hydrogenated Alcohols Using Perfluorinated tert-Butanol: A Multitechnique Approach (Infrared, Raman, and X-ray Scattering) Analyzed by DFT and Molecular Dynamics Calculations. *J. Phys. Chem. B* **2022**, *126*, 1992−2004.

(62) Kiefer, J.; Wagenfeld, S.; Kerlé, D. Chain Length Effects on the Vibrational Structure and Molecular Interactions in the Liquid Normal Alkyl Alcohols. *Spectrochim. Acta A Mol. Biomol. Spectrosc.* **2018**, *189*, 57−65.

(63) Kalhor, P.; Li, Q.-Z.; Zheng, Y.-Z.; Yu, Z.-W. Is the Fourier Transform Infrared Free-OH Band of t-Butanol Only from Free OHs? Case Studies on the Binary Systems of the Alcohol with CCl_4 and $CHCl_3$. *J. Phys. Chem. A* **2020**, *124*, 6177−6185.

(64) Graener, H.; Ye, T. Q.; Laubereau, A. Ultrafast Dynamics of Hydrogen Bonds Directly Observed by Time-resolved Infrared Spectroscopy. *J. Chem. Phys.* **1989**, *90*, 3413−3416.

(65) Lutz, B. T.; Langoor, M. H.; van der Maas, J. H. The Sensorial Potentials of the OH-stretching Mode: Phenols. *Vib. Spectrosc.* **1998**, *18*, 111−121.

(66) Orendorff, C. J.; Ducey, M. W. J.; Pemberton, J. E. Quantitative Correlation of Raman Spectral Indicators in Determining Conformational Order in Alkyl Chains. *J. Phys. Chem. A* **2002**, *106*, 6991−6998.

(67) Liao, Z.; Pemberton, J. E. Raman Spectral Conformational Order Indicators in Perdeuterated Alkyl Chain Systems. *J. Phys. Chem. A* **2006**, *110*, 13744−13753.

(68) Rich, A. M.; Bhattacharyya, S.; Aldilla, V. R.; Beves, J. E.; Bhadbhade, M.; Kumar, N.; Luis, E. T.; Marjo, C. E. Quantifying Alkyl Chain Disorder in Crystalline Models of Lipid Bilayers Using Raman Spectroscopy. *J. Raman Spectrosc.* **2019**, *50*, 63−73.

(69) Blackledge, M. NMR Provides Evidence for Dynamic Hydrogen Bonding in Proteins. *Protein Sci.* **2007**, *16*, 1247−1248.

(70) Posada, E.; Roldán-Ruiz, M.; Jiménez Riobóo, R.; Gutiérrez, M.; Ferrer, M.; del Monte, F. Nanophase Separation in Aqueous Dilutions of a Ternary DES as Revealed by Brillouin and NMR Spectroscopy. *J. Mol. Liq.* **2019**, *276*, 196−203.

(71) Veroutis, E.; Merz, S.; Eichel, R. A.; Granwehr, J. Intra- and Inter-molecular Interactions in Choline-based Ionic Liquids Studied by 1D and 2D NMR. *J. Mol. Liq.* **2021**, *322*, 114934.

(72) Triolo, A.; Di Pietro, M. E.; Mele, A.; Lo Celso, F.; Brehm, M.; Di Lisio, V.; Martinelli, A.; Chater, P.; Russina, O. Liquid Structure and Dynamics in the Choline Acetate:Urea 1:2 Deep Eutectic Solvent. *J. Chem. Phys.* **2021**, *154*, 244501.

(73) Herschlag, D.; Pinney, M. M. Hydrogen Bonds: Simple after All? *Biochem* **2018**, *57*, 3338−3352.